# Reflection-type infrared biosensor based on surface plasmonics in graphene ribbon arrays

**Wei Wei (韦 玮)**[1,2,3,4,*], **Jinpeng Nong (农金鹏)**[1,2], **Linlong Tang (汤林龙)**[3,4], **Guiwen Zhang (张桂稳)**[1,2], **Xiao Jiang (蒋 肖)**[1,2], and **Yong Zhu (朱 永)**[1,2,4]

[1]*Key Laboratory of Optoelectronic Technology & Systems, Ministry of Education of China, Chongqing University, Chongqing 400044, China*

[2]*College of Optoelectronic Engineering, Chongqing University, Chongqing 400044, China*

[3]*Chongqing Institute of Green and Intelligent Technology, Chinese Academy of Sciences, Chongqing 401122, China*

[4]*Chongqing Engineering Research Center of Graphene Film Manufacturing, Chongqing 401329, China*

*Corresponding author: wwei@cqu.edu.cn*

We propose a reflection-type infrared biosensor by exploiting localized surface plasmons in graphene ribbon arrays. By enhancing the coupling between the incident light and the resonant system, an asymmetric Fabry–Perot cavity formed by the ribbons and reflective layer is employed to reshape the reflection spectra. Simulation results demonstrate that the reflection spectra can be modified to improve the figure of merit (FOM) significantly by adjusting the electron relaxation time of graphene, the length of the Fabry–Perot cavity, and the Fermi energy level. The FOM of such a biosensor can achieve a high value of up to 36/refractive index unit (36/RIU), which is ~4 times larger than that of the traditional transmission-type one. Our study offers a feasible approach to develop biosensing devices based on graphene plasmonics with high precision.

OCIS codes: 280.1415, 240.6680, 160.4236, 260.3060.
doi: 10.3788/COL201513.082801.

Surface plasmon resonance (SPR), the electromagnetic excitations that propagate along the metal-dielectric interface, is the pillar stone of ultrasensitive optical biosensing[1–3]. While much progress has been made in engineering SPR biosensors with noble metals[4–7] at visible and near-infrared frequencies, a bottleneck arises when further pushing the SPR frequencies into mid- and far-infrared. At these frequencies, SPR waves are weakly confined to the metallic surface due to the increasing negative permittivity[8], which limits the sensitivity of the SPR biosensor. Moreover, the high surface inertness and intrinsic hydrophobicity make it unable to adsorb biomolecules on metal ideally[9], and the large surface electric density also restrains the possibility of tuning the plasmon energy via external electrostatic fields[10]. These defects that are determined by the nature of the metal material hinder the future development of infrared SPR biosensors.

In contrast to metal, graphene that emerged as a 2D material[11] supports propagating surface plasmon polaritions at infrared and terahertz frequencies[12,13]. Its surface conductivity can be controlled by the external electric field[14], making it a promising candidate for actively controlled plasmonics sensors[15]. Moreover, the biomolecules can be effectively adsorbed on its surface owing to the high surface-to-volume ratio and $\pi$-$\pi$ stacking between the graphene and the carbon-based ring structures in biomolecules[16,17]. Very recently, various biosensors based on graphene ribbon arrays (GRAs) have been theoretically investigated[18–20]. The simulation results show that a high sensitivity can be acquired by designing a large period and width of the GRA. However, the enhancement of the sensitivity caused by the redshift of the resonant wavelength is always accompanied by the broadening of the resonance dip[18–20]. Such behavior dramatically reduces the precision of the biosensor; namely, the figure of merit (FOM) of the GRA biosensor is very low for sensing applications, which immensely restricts the evolution of the infrared graphene biosensor. In this Letter, we propose a reflection-type infrared biosensor employing a metallic reflective layer to enhance the coupling between the incident light and the device and focus on the significant improvement of the FOM by reshaping the spectral line.

The proposed infrared biosensor is schematically shown in Fig. 1(a). The GRA is covered on the top of the dielectric spacer, on which the bottom is deposited a thick gold film as a reflective layer. $\Lambda$ is the period of the GRA, $W$ is the width of the ribbon, and $T$ is the thickness of the spacer. $n_d$ is the refractive index of medium above the graphene. The permittivity of the spacer is
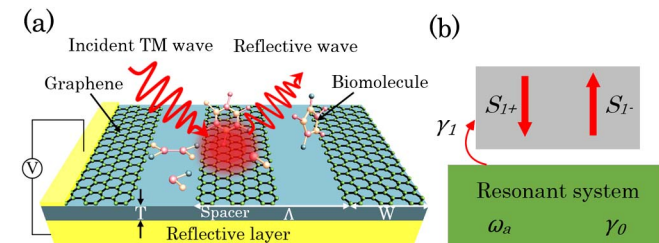


Fig. 1. (a) Schematic of the biosensor based on graphene plasmonics and (b) the temporal coupled theory description of the coupling among the incident light, reflected light and the device.

$\varepsilon_{\mathrm{spa}} = 2.25$ and the permittivity of gold is extracted from the reference[21]. Simulations are carried out by the finite element method employing Comsol mutiphysics. Graphene is modeled as a thin monolayer with a thickness of 0.34 nm. The mesh size inside the graphene layer along the $Z$ axis is 0.03 nm and the mesh size gradually increases outside the graphene. The intraband surface conductivity of graphene at the midinfrared frequencies follows the Drude model as[22]

$$\sigma(\omega) = \frac{e^2 E_f}{\pi \hbar^2} \frac{i}{\omega + i\tau^{-1}}, \qquad (1)$$

where $\omega$ is the angular frequency of the incident TM wave, $e$ is the elementary charge, $\hbar$ is the reduced Plank constant, $E_f$ is the Fermi energy, and $\tau$ is the electron relaxation time. The dispersion relation of the graphene plasmonics (GPs) mode for TM incident light can be expressed as

$$q(\omega) = \frac{\pi \hbar^2 \varepsilon_0 (\varepsilon_{\mathrm{spa}} + \varepsilon_n)}{e^2 E_f} (1 + i/\omega\tau)\omega^2, \qquad (2)$$

Under normal-incidence of light, a GPs wave can be excited once the reciprocal lattice vector of the GRA matches the resonant condition $\mathrm{Re}(q(\omega)) = 2\pi m/\Lambda$, where $m = 1$ represents the GPs mode excited by the first diffraction order of the GRA. The excited GPs mode pattern is shown in Fig. 2(a). One can see that the excitation of the GPs wave exhibits a strong ability to confine free space light to subwavelength spots, creating a strong light-matter interaction within the near-field region. Due to the ohmic loss of the propagating GPs wave, a dip can be observed in the reflection spectrum and its resonant wavelength $\lambda_{\mathrm{GPs}}$ can be expressed as

$$\lambda_{\mathrm{GPs}} = \frac{\pi \hbar c}{e} \sqrt{\frac{2\varepsilon_0 (\varepsilon_{\mathrm{spa}} + \varepsilon_n)\Lambda}{E_f}}. \qquad (3)$$

The appearance of the biomolecules will lead to a refractive index change near the graphene interface, which results in the shift of the resonant wavelength. One can
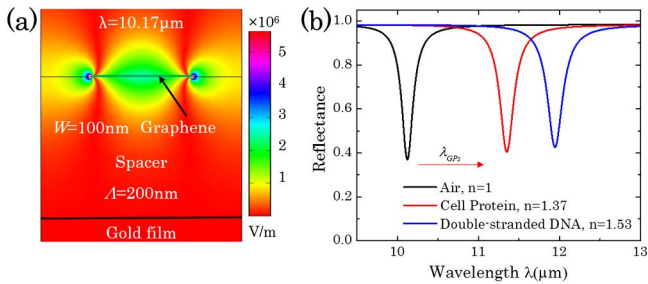


Fig. 2. (a) Calculated GPs mode pattern when $\Lambda = 200$ nm and $W = 100$ nm and (b) reflection spectra with sensing medium change from air to cell protein ($n = 1.37$) and to double-stranded DNA ($n = 1.53$).

see in the reflection spectra in Fig. 2(b) that the resonant wavelength redshifts from 10.17 to 11.30 μm as the sensing medium changes from air to cell protein. Then the sensitivity of the biosensor is 3067 nm/refractive index unit (RIU), which is calculated

$$S = \frac{\delta\lambda_{\mathrm{GPs}}}{\delta n_d} = \frac{\pi \hbar c}{e} \sqrt{\frac{2\varepsilon_0 \Lambda}{E_f}} \frac{n_d}{\sqrt{n_d^2 + \varepsilon_{\mathrm{spa}}}}. \qquad (4)$$

To realize a high detection precision in practice, a narrower and deeper resonant notch of the reflection spectrum is highly desired[19]. Thus, the FOM is employed to assess this performance of the sensor, which can be expressed as

$$\mathrm{FOM} = \frac{S}{\mathrm{FWHM}}(1 - R_a), \qquad (5)$$

where FWHM is the full width at half-maximum of the resonant curves, and $R_a$ is the reflectance at the resonant frequency. Obviously, the key to improve the FOM is reshaping the reflection spectral line.

To explore the essential parameters that determine the spectral line shape, a physical model based on temporal coupled mode theory is built, as sketched in Fig. 1(b). The resonant system couples with the incident and reflected light and it can be characterized using the temporal coupled mode equations[23] as follows:

$$\frac{da}{dt} = -(i\omega_a + \gamma_0 + \gamma_1)a + \sqrt{2\gamma_1}S_{1+}, S_{1-} = \sqrt{2\gamma_1}a - S_{1+}, \qquad (6)$$

where $a$ is the amplitude of a GPs mode, $\gamma_0$ is the intrinsic loss rate, $\gamma_1$ is the leakage rate, $\omega_a$ is the resonant frequency, and $S_{1+}$ and $S_{1-}$ are the amplitudes of the incident and reflected light, respectively. The reflectance of resonant system can be derived as

$$R = \left| \frac{S_{1-}}{S_{1+}} \right|^2 = \frac{(\omega - \omega_a)^2 + (\gamma_0 - \gamma_1)^2}{(\omega - \omega_a)^2 + (\gamma_0 + \gamma_1)^2}. \qquad (7)$$

Then, the reflectance at the resonant frequency $\omega_a$ is obtained as $R_a = (\gamma_0 - \gamma_1)^2/(\gamma_0 + \gamma_1)^2$, and the FWHM gives us $2(\gamma_0 + \gamma_1)$[24]. By substituting them into Eq. (5), the FOM is given by $2S\gamma_0\gamma_1/(\gamma_0 + \gamma_1)^3$. The intrinsic loss rate $\gamma_0$ is determined by the relaxation time $\tau$ of graphene through $\gamma_0 \approx 1/(2\tau)$ in the considered infrared region, while the leakage rate $\gamma_1$ is decided by the spacer thickness $T$. Therefore, tuning $\tau$ and $T$ can reshape the spectral line to improve the FOM.

In the following, the influence of the relaxation time $\tau$ of graphene on the FOM is investigated. The reflection spectra with varying $\tau$ are shown in Fig. 3(a). One can see that the spectral line can be modified by adjusting the electric property of graphene. Specifically, the bandwidth of the resonant dip becomes narrower and the resonant depth
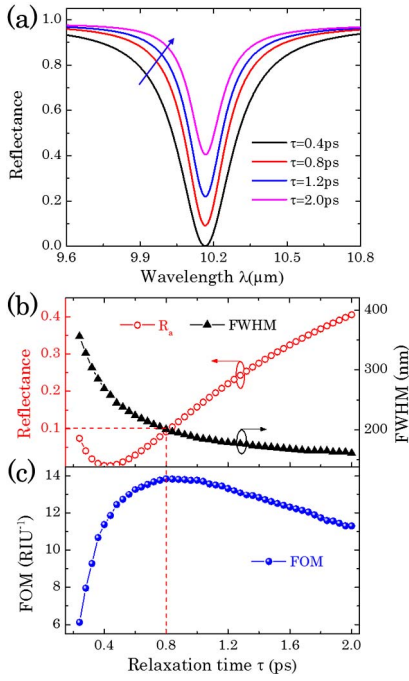
Fig. 3. (a) Simulated reflection spectra with varying $\tau$ when $T = 800$ nm. (b) Resonant reflectance and FWHM extracted from the reflection spectra with varying $\tau$. (c) Calculated FOM as a function of $\tau$.
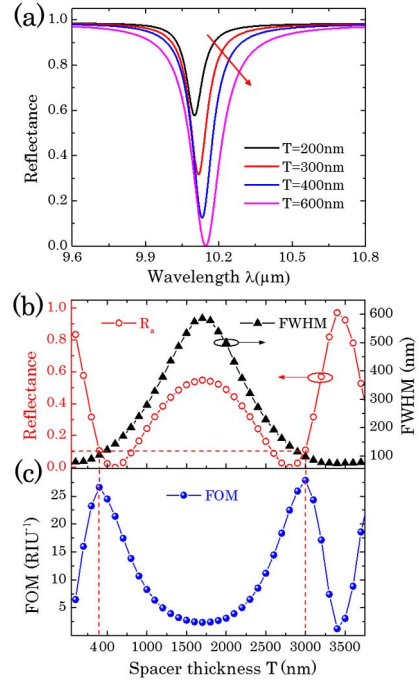


Fig. 4. (a) Simulated reflection spectra with varying $T$ when $\tau = 0.8$ ps. (b) Resonant reflectance and FWHM extracted from the reflection spectra with varying $T$. (c) Calculated FOM as a function of $T$.

becomes shallower with increasing $\tau$ from 0.4 to 2 ps. The characteristic parameters, $R_a$ and FWHM, that quantitatively determine the spectral line shape are extracted from Fig. 3(a) and plotted in Fig. 3(b). As a result, the FOM can be adjusted over a wide range, as indicated in Fig. 3(c) and can be improved by 2.3 times from 6.01/RIU to a maximum value of 13.85/RIU as $\tau$ increases from 0.2 to 0.8 ps.

The impact of the spacer thickness $T$ on the FOM is also investigated. The reflection spectra for some selected value of $T$ are shown in Fig. 4(a). They show that the notch becomes broader and deeper as $T$ varies from 200 to 600 nm. The $R_a$ and FWHM are further extracted from the spectra in a wider range of $T$ and shown in Fig. 4(b). The results reveal that $R_a$ and FWHM vary periodically with $T$, which consequently lead to the variation of FOM with the same period as shown in Fig. 4(c). Two maximum FOMs of 27.43/RIU can be obtained with an interval of 2600 nm in a period. Such a periodic variation can be explained by considering the device as an asymmetric Fabry–Perot cavity[25] in which the GRA and the gold layer are the top mirror and the bottom mirror, respectively. According to the Fabry–Perot physical model, the predicting variation period as a function of the resonant wavelength and permittivity of the spacer is obtained as $T_0 = \lambda_{\mathrm{GPs}}/2(\varepsilon_{\mathrm{spa}})^{1/2}$, which is in good agreement with the simulation results. Therefore, the FOM can achieve the maximum value by selecting the suitable length of the Fabry–Perot cavity in the initial design.

It is worth noting that the FOM reaches the maximum value when the reflectance is not zero but $R_a \approx 11\%$. Namely, the perfect absorption is not the optimal option for improving the FOM, although it is desired commonly for a GPs device[26]. This phenomenon can be interpreted as follows: according to the first order derivative of formula $\mathrm{FOM} = 2S\gamma_0\gamma_1/(\gamma_0 + \gamma_1)^3$, two solutions exist to obtain the maximum; i.e., $\gamma_0 = \gamma_1/2$ for a fixed $\gamma_1$, or $\gamma_0 = 2\gamma_1$ for a fixed $\gamma_0$. By substituting these solutions into $R_a = (\gamma_0 - \gamma_1)^2/(\gamma_0 + \gamma_1)^2$ we arrive at the same reflectance $R_a \approx 11\%$ in both cases. Therefore, the FOM can be improved to the maximum value by satisfying the condition of $R_a \approx 11\%$ either by modulating $\tau$ or $T$. The above analysis provides us guidance to tune the FOM in practical applications. The relaxation time of graphene is relatively difficult to tune because it is the intrinsic property of graphene. Nevertheless, we can always adjust the spacer thickness to meet the condition of $R_a \approx 11\%$ in order to maximize the FOM.

We further investigate the influence of the Fermi energy level $E_f$ of graphene on the performance of the biosensor. By adjusting the gate voltage of the device, the reflection spectra can be tuned over an ultrabroad range. The reflectance mapping with varying wavelength of incident light and Fermi energy level is illustrated in Fig. 5(a). It presents the blueshift of the resonant wavelength $\lambda_{\mathrm{GPs}}$ from 11.68 to 9.05 μm as $E_f$ increases from 0.3 to 0.5 eV, along with the decrease of the FWHM from 120 to 100 nm. To visually illustrate the variation of the spectral line, the reflection spectra with several sets of $E_f$ are
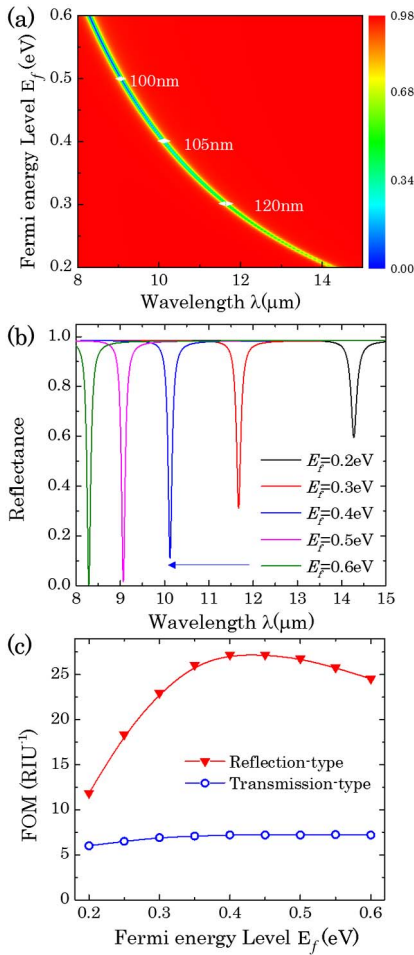
Fig. 5. (a) Reflectance mapping with varying wavelength of incident light and Fermi energy level when $T = 400$ nm and $\tau = 0.8$ ps. (b) The extracted reflection spectra with varying Fermi energy level of graphene from 0.2 to 0.6 eV. (c) Comparison of the FOM of the reflection-type and the transmission-type biosensors with varying Fermi energy level.

extracted and given in Fig. 5(b). It can be seen that the spectral line becomes narrower and deeper monotonously with the increase of $E_f$. The variation of the reflection spectra results in the dramatic variation of the FOM of the proposed biosensor, as plotted in Fig. 5(c). However, the FOM does not vary monotonously; instead, it initially exhibits an increase and then a decrease tendency after reaching a maximum value of 27.43/RIU when $E_f = 0.4$ eV. This is the result of the variation of $\gamma_1$ induced by the shift of $\lambda_{\mathrm{GPs}}$ with varying $E_f$ for a fixed $T$. Only when the Fermi energy level $E_f$ is adjusted to match the condition of $\gamma_0 = 2\gamma_1$ ($R_a \approx 11\%$), can the FOM reach its maximum value. Furthermore, the corresponding FOMs are compared with that of the transmission-type biosensors of the same parameters of the GRA in Fig. 5(c). Obviously, the FOM of the proposed reflection-type biosensor is much larger than that of the transmission-type one, and by adjusting the Fermi energy level of graphene, the FOM of the proposed biosensor can be improved after the fabrication of the device.
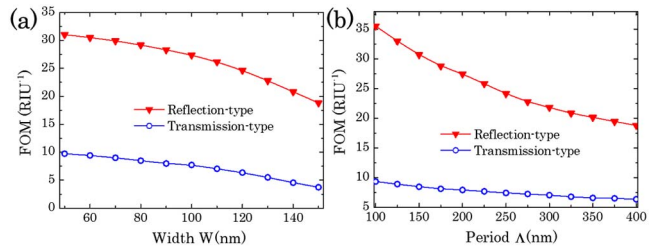


Fig. 6. Comparison of the FOM of the reflection-type and the transmission-type biosensors with varying width (a) for a fixed $\Lambda = 200$ nm and period (b) for a fixed occupation ratio of 50%.

Finally, the FOM of the proposed biosensors with varying width $W$ and period $\Lambda$ of the GRA are calculated and compared with that of the transmission-type biosensor. For the transmission-type one, the resonant wavelength redshifts to the longer wavelength region as $W$ and $\Lambda$ increase, along with the broadening of the resonance dip. This leads to the decrease of the FOM for both cases, which is in agreement with the result in references[18–20]. While for each proposed reflection-type structure, we fix $\tau = 0.8$ ps and only adjust $T$ to satisfy $R_a \approx 11\%$ in the initial device design process. The optimized FOM of the structures with different $W$ and $\Lambda$ are represented by the red lines in Figs. 6(a) and 6(b), respectively. It can be seen that the reflection-type biosensor gains an obvious advantage over the transmission-type biosensor. The FOM of the reflection-type biosensor can be improved by 65% from 18.83/RIU to 31.03/RIU as $W$ decreases from 150 to 50 nm and by 97% from 18.18/RIU to 36/RIU as $\Lambda$ decreases from 400 to 100 nm. Particularly in the case of $\Lambda = 100$ nm, the FOM of the reflection-type biosensor is ~4 times larger than that of the transmission-type one. In this case the sensitivity of the reflection-type biosensor ($S = 2270$ nm/RIU) calculated from Eq. (4) is also larger than that of the transmission-type one ($S = 2204$ nm/RIU). Therefore, with respect to the transmission-type biosensor, the FOM of the reflection-type biosensor can be significantly improved while maintaining its high sensitivity.

In conclusion, a reflection-type infrared biosensor based on surface plasmonics in GRAs is proposed. The physical parameters that dominate the spectral line shape are revealed. Simulation results indicate that reshaping the resonant curves can improve the FOM of a biosensor to a maximum value. Furthermore, the detection precision of the proposed biosensor gains a great advantage over the transmission-type biosensors. These proposed biosensing strategies may be useful for developing novel biosensors based on GPs with high precision.

## References

1. Y. Wu, Chin. Opt. Lett. **12**, 110607 (2014).
2. H. Yang, W. Lee, T. Hwang, and D. Kim, Opt. Express **22**, 28412 (2014).
3. M. Abb, Y. Wang, N. Papasimakis, C. H. de Groot, and O. L. Muskens, Nano Lett. **14**, 346 (2014).
4. D. Zhang, Y. Lu, J. Jiang, Q. Zhang, Y. Yao, P. Wang, B. Chen, Q. Cheng, G. L. Liu, and Q. Liu, Biosens. Bioelectron. **67**, 237 (2015).
5. T. Wang, V. H. Nguyen, A. Buchenauer, U. Schnakenberg, and T. Taubner, Opt. Express **21**, 9005 (2013).
6. X. Wang, F. Liu, A. Liu, B. Fan, K. Cui, X. Feng, W. Zhang, and Y. Huang, Chin. Opt. Lett. **12**, 010602 (2014).
7. A. H. Nguyen, X. Ma, and S. J. Sim, Biosens. Bioelectron. **66**, 497 (2015).
8. S. Law, L. Yu, A. Rosenberg, and D. Wasserman, Nano Lett. **13**, 4569 (2013).
9. S. H. Choi, Y. L. Kim, and K. M. Byun, Opt. Express **19**, 458 (2011).
10. V. W. Brar, M. S. Jang, M. Sherrott, J. J. Lopez, and H. A. Atwater, Nano Lett. **13**, 2541 (2013).
11. K. S. Novoselov, V. I. Fal'ko, L. Colombo, P. R. Gellert, M. G. Schwab, and K. Kim, Nature **490**, 192 (2012).
12. H. Yan, X. Li, B. Chandra, G. Tulevski, Y. Wu, M. Freitag, W. Zhu, P. Avouris, and F. Xia, Nat. Nanotechnol. **7**, 330 (2012).
13. D. Jin, A. Kumar, K. Hung Fung, J. Xu, and N. X. Fang, Appl. Phys. Lett. **102**, 201118 (2013).
14. J. Niu, Y. Jun Shin, Y. Lee, J.-H. Ahn, and H. Yang, Appl. Phys. Lett. **100**, 061116 (2012).
15. Y. Li, H. Yan, D. B. Farmer, X. Meng, W. Zhu, R. M. Osgood, T. F. Heinz, and P. Avouris, Nano Lett. **14**, 1573 (2014).
16. V. Georgakilas, M. Otyepka, A. B. Bourlinos, V. Chandra, N. Kim, K. C. Kemp, P. Hobza, R. Zboril, and K. S. Kim, Chem. Rev. **112**, 6156 (2012).
17. D. Feng, G. Liu, M. Zhang, and D. Jia, Chin. Opt. Lett. **11**, 110607 (2013).
18. J. Wu, C. Zhou, J. Yu, H. Cao, S. Li, and W. Jia, Opt. Laser Technol. **59**, 99 (2014).
19. Y. Zhao, X. Hu, G. Chen, X. Zhang, Z. Tan, J. Chen, R. S. Ruoff, Y. Zhu, and Y. Lu, Phys. Chem. Chem. Phys. **15**, 17118 (2013).
20. B. Vasić, G. Isić, and R. Gajić, J. Appl. Phys. **113**, 013110 (2013).
21. E. D. Palik and G. Ghosh, *Handbook of Optical Constants of Solids* (Academic, 1985).
22. W. Gao, J. Shu, C. Qiu, and Q. Xu, ACS Nano **6**, 7806 (2012).
23. L. Tang, J. Du, C. Du, P. Zhu, and H. Shi, Opt. Express **22**, 20214 (2014).
24. J. R. Piper and S. Fan, ACS Photonics **1**, 347 (2014).
25. R. Alaee, M. Farhat, C. Rockstuhl, and F. Lederer, Opt. Express **20**, 28017 (2012).
26. Z. Fang, Z. Liu, Y. Wang, P. M. Ajayan, P. Nordlander, and N. J. Halas, Nano Lett. **12**, 3808 (2012).